Cadatal-Raduban et al. *NPG Asia Materials* (2024) 16:50
https://doi.org/10.1038/s41427-024-00570-8

NPG Asia Materials

ARTICLE Open Access

Pressure-controlled luminescence in fast-response barium fluoride crystals

Marilou Cadatal-Raduban[1,2,3], Luong Viet Mui[4], Masahiro Yamashita[2,4], Yuki Shibazaki[5], Toshihiko Shimizu[2], Nobuhiko Sarukura[2,6] and Kohei Yamanoi[2]

Abstract

Cross-luminescence (CL) in a barium fluoride (BaF_2) scintillator arising from the recombination of a valence band electron and a core band hole results in a fast picosecond decay time. However, the CL emission wavelength in the vacuum ultraviolet region is difficult to detect, and intrinsically intense and slow nanosecond self-trapped exciton (STE) luminescence occurs. Herein, we report a redshift in the CL emission wavelength with high-pressure application. The wavelength of the CL emission shifted from 221 nm to 240 nm when 5.0 GPa was applied via a sapphire anvil cell. Increasing the pressure decreases the core-valence bandgap due to the downward expansion of the valence band, resulting in a decrease in the valence band minimum. The onset of a phase transition from a cubic crystal structure to an orthorhombic crystal structure at 3.7 GPa inhibited the recombination of conduction band electrons and self-trapped holes, leading to the disappearance of the STE emission. Manipulating the band structure of BaF_2 by high-pressure application enables control of its luminescence emission, providing a pathway toward solving the problems inherent in this leading fast-response scintillator.

Introduction

Ionizing radiation is ubiquitous in many applications. High-energy photons, gamma rays, X-rays, neutrons, and charged particles are being harnessed in many applications, such as nuclear medicine, border security, mineral and oil exploration, and nuclear fusion research. The detection and monitoring of ionizing radiation rely on an intermediary material, called a scintillator, which subsequently emits photons after absorbing the radiation. The scintillator therefore converts the otherwise inaccessible ionizing radiation into light, called luminescence, which can be detected by photodetectors. Luminescence from a scintillator originates from the energy-level transitions of excited electrons[1]. As such, many scintillators have been developed using crystals and glasses doped with rare-earth activator ions such as cerium[2–4], praseodymium[5–7], neodymium[8], gadolinium[9], and lutetium[9]. Wide-band-gap fluorides, silicates, orthosilicates, and borates are among the host materials doped with rare-earth ions, depending on the required density and stopping power for the radiation of interest. In these rare-earth-doped scintillators, luminescence originates from electronic transitions between the excited state energy levels and the ground state energy levels that are established by crystal-field splitting within the forbidden gap between the conduction and valence bands of the host material. For trivalent rare-earth ions, radiative decay occurs from the lowest level of their excited $4f^{n-1}5d$ electronic configuration (often referred to as the lowest 5d level for simplicity) to the ground state and some excited levels of the ground $4f^n$ electronic configuration (often referred to as the 4f level for simplicity)[9]. If the transition is parity-allowed, the resulting luminescence will have a fast decay time that is typically in the nanosecond range, as was observed in the lithium yttrium fluoride ($LiYF_4$) host crystal doped with trivalent cerium, praseodymium, gadolinium, and lutetium[9]. However, in many applications, a fast picosecond luminescence decay time is desired. Time-of-flight (TOF) detectors, for example, in particle detection, TOF-positron emission tomography (TOF-PET), and nuclear

Correspondence: Kohei Yamanoi (yamanoi.kohei.ile@osaka-u.ac.jp)
[1]Unitec Institute of Technology, 139 Carrington Road, Mount Albert, Auckland 1025, New Zealand
[2]Institute of Laser Engineering, Osaka University, 2-6 Yamadaoka, Suita, Osaka 565-0871, Japan
Full list of author information is available at the end of the article

fusion research, rely on the scintillator's fast decay time to discriminate between different types of radiation that exist simultaneously. High-resolution nuclear imaging cameras and high-rate ultrafast timing devices also require scintillators with picosecond decay times[10]. Along with a fast decay time, a high light yield is needed for ease of detection of the luminescence signal. However, scintillator materials are limited to one feature or the other because of the trade-off between decay time and light yield. The problem of detecting weak luminescence from a scintillator with low light yield can be solved by using multiple detector arrays[11]. However, obtaining a fast luminescence decay time poses a more fundamental problem that is more difficult to solve. Several schemes, including luminescence quenching via high doping concentrations[12] and energy transfer by co-doping[13], have been investigated to achieve fast luminescence decay times via rare-earth-doped materials. However, picosecond decay times are not achievable via these schemes. Additionally, the presence of parity-forbidden transitions in rare-earth-doped materials introduces a very slow luminescence component with decay times on the order of milliseconds to microseconds.

Picosecond decay times can be achieved in materials exhibiting core-to-valence luminescence (CVL) or cross-luminescence (CL), also sometimes referred to as Auger-free luminescence. CL occurs because of the radiative recombination of electrons from the valence band with the holes in the uppermost core band, with the holes being created when the crystal is irradiated with radiation whose energy exceeds the ionization edge of the uppermost core band. In most crystals, the hole created in the uppermost core band decays nonradiatively via Auger decay. In this case, an electron from the valence band recombines with the hole in the core band, and the energy released is transferred non radiatively to another electron in the valence band, which then escapes to the conduction band[9]. However, Auger decay does not occur in some crystals whose uppermost core band lies at a high energy such that the energy difference between the tops of the valence and uppermost core bands is less than the bandgap energy of the crystal. In this case, radiative recombination of the core hole with the valence electron dominates and results in CVL emission[9]. Since Auger decay has not occurred, CVL is also called Auger-free luminescence. The term CL reflects the fact that at the CL transition, the electron is transferred from one ion (anion) to another ion (cation) because, in ionic crystals, the valence band is formed from the *p*-type states of the anion and the uppermost core band is formed from the *p*-type states of the cation[9]. CL has been observed in BaF_2, LaF_3, $KMgF_3$, and $BaLiF_3$[14–17]. For CL in BaF_2, the incident radiation promotes an electron in the filled $5p$ Ba^{2+} core band to the empty $6s$, $5d$ Ba^{2+} conduction band, leaving behind a hole in the core band that then relaxes to the core band edge (see Fig. 1). An electron in the filled $2p$ F^- valence band recombines with this hole in the core band, resulting in the CL emission[14,15,17]. Afterward, the electron initially promotes the conduction band, and the hole remaining in the valence band after CL recombines via self-trapped exciton (STE) formation. This results in slow STE luminescence emission with a decay time of a few hundred nanoseconds, which deteriorates the picosecond decay time of CL and should therefore be suppressed. Since CL emission arises from band-to-band transitions, the lifetime of the transition is very short, and the luminescence decay times are a few hundred picoseconds (600 ps in BaF_2, 270 ps in $KMgF_3$, and 300 ps in $BaLiF_3$)[16,18]. Recently, observations of shorter CL emission in the range of 100 ps have been reported[19,20]. The caveat is that the wavelength of picosecond CL emission is in the vacuum ultraviolet (VUV) wavelength region. It is difficult to detect CL emission not only because of its high energy but also because VUV wavelengths are absorbed by oxygen in air. As such, conventional photodetectors cannot be used to detect CL, and measurements need to be performed under vacuum or nitrogen purging unless the CL emission wavelength can be shifted to a longer wavelength. Additionally, the majority of the light output (for example, ~80% of the light output from BaF_2) occurs in the slow STE component[21]. Despite these difficulties, the BaF_2 single crystal is still the leading fast-response scintillator on the market because of its picosecond-CL emission. Owing to its practical use as a fast scintillator material, BaF_2 is the ideal material for fundamental research on CL, with the aim of shifting fast CL emission to longer wavelengths and suppressing slow STE emission. Shifting the CL of BaF_2 to a longer wavelength involves manipulation of its electronic structure to decrease the energy gap between the valence and core bands. Here, we manipulate the band structure of BaF_2 through high-pressure application to control the energy

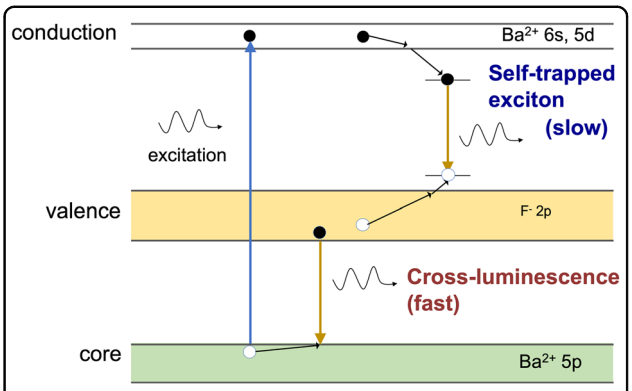

Fig. 1 Transitions leading to CL in BaF_2 crystal. Schematic diagram of the mechanisms for CL and STE luminescence emission in BaF_2.

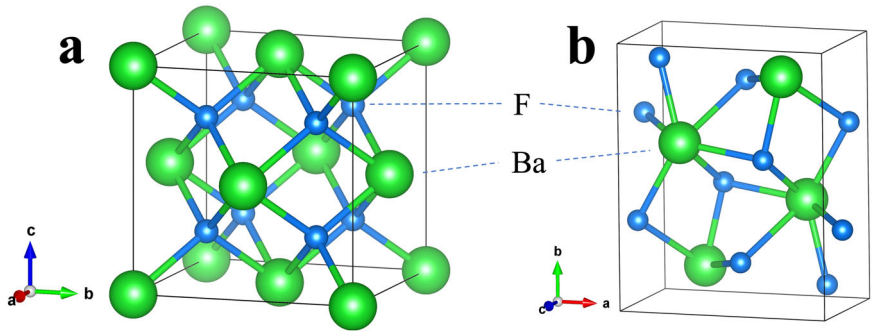

Fig. 2 Crystal structures of BaF_2. a Cubic phase. **b** Orthorhombic phase.

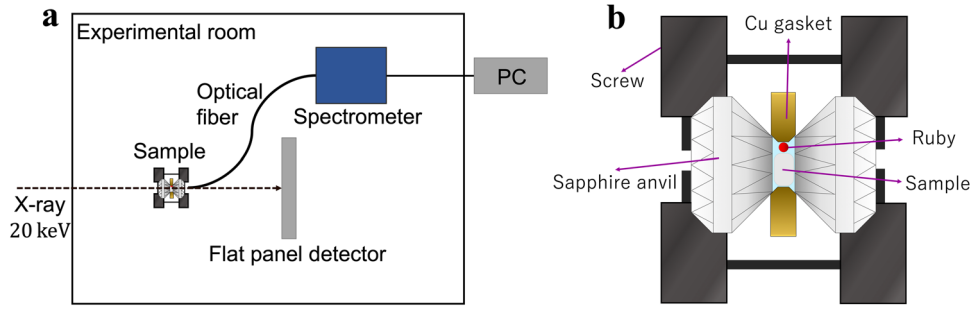

Fig. 3 Luminescence and XRD measurements under high pressure. a Schematic diagram of the high-pressure experimental setup. **b** Details of the sapphire anvil cell used to apply high pressure.

gap between the first core band and the valence band, thereby tuning its CL emission wavelength. By compressing the crystal using pressures up to 8.7 GPa, we investigate changes in the BaF_2 electronic structure; changes in its conduction, valence, and first core bands; and changes in its bandgap energies.

Results and discussion

The effects of pressure on the electronic structure and bandgap energies correlate with experimentally observed changes in the CL and STE luminescence emissions. At ambient (0 GPa) pressure, BaF_2 has a cubic phase with a lattice constant $a = 6.2$ Å (Fig. 2a). It belongs to the space group Fm-3m (group number 225)[21–23]. Ba^{2+} ions exhibit a bonding arrangement within a body-centered cubic structure, wherein they are surrounded by eight identical F^- ions. The distance between the Ba and F ions in these bonds is 2.70 Å. Each F^- ion forms bonds with four equivalent Ba^{2+} ions, resulting in the creation of a combination of FBa_4 tetrahedra through a combination of corner- and edge-sharing interactions. The atomic coordinates for Ba and F are (0.0, 0.0, 0.0) and (0.25, 0.25, 0.25), respectively. The BaF_2 crystal is placed in a sapphire anvil cell and is excited by 20 keV synchrotron radiation X-rays, as shown in the schematic diagram of the experimental setup in Fig. 3. A sapphire anvil cell is used instead of the more durable and commonly used diamond anvil cell because the CL emission from BaF_2 at ambient pressure is expected to be ~200 nm. Diamond is opaque, whereas sapphire is transparent down to ~150 nm[24,25]. The luminescence from BaF_2 under pressure is detected via a fiber spectrometer. X-ray diffraction (XRD) measurements were performed simultaneously via 20 keV synchrotron radiation X-rays. Figure 4a shows the XRD patterns of BaF_2 at pressures ranging from 0.1 GPa (approximately ambient) to 8.7 GPa. At 0.1 GPa, the peaks can be indexed to the cubic phase of BaF_2 with a dominant orientation along the [111] plane. The cubic crystal structure is maintained at a pressure of ~2 GPa (Fig. 4b). Above 4.5 GPa, the XRD peaks can be indexed to the orthorhombic phase of BaF_2 (Fig. 4d). The [111] plane is still the dominant orientation in the orthorhombic phase. In the orthorhombic phase, BaF_2 belongs to the space group Pnam (group number 62)[21–23]. Ba^{2+} ions are engaged in a 9-coordinate geometry and surrounded by nine F^- ions. The Ba–F bond distances are variable, ranging from 2.61 to 3.02 Å. There are two distinct F^- sites. In the first site, F^- forms bond within a 5-coordinate arrangement to five identical Ba^{2+} ions. Moreover, at the second F^- site, F^- forms bond with four equivalent Ba^{2+} ions, leading to the formation of a mixture of FBa_4 tetrahedra through a combination of edge- and corner-

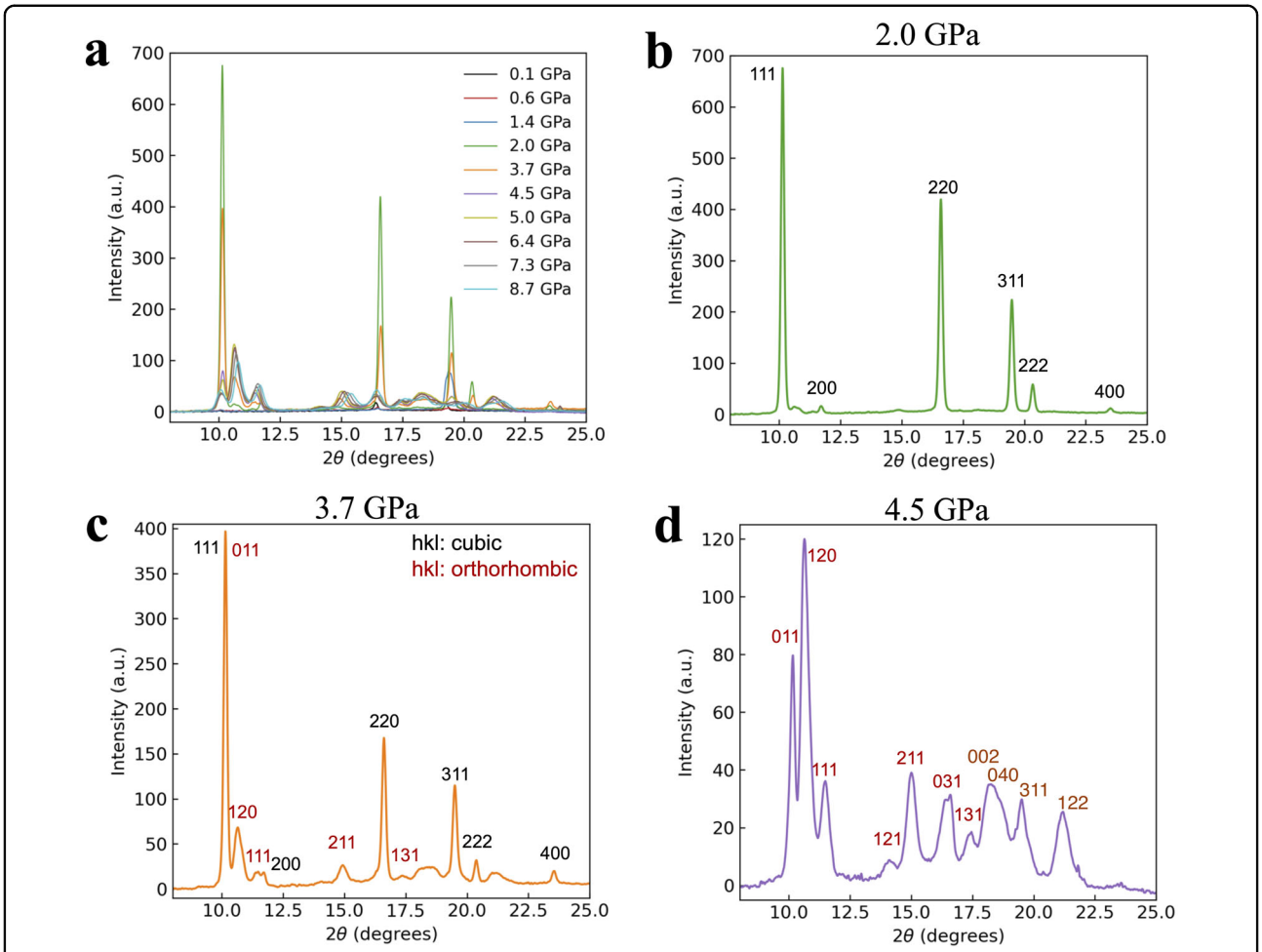

Fig. 4 XRD spectra of BaF_2. **a** XRD pattern from 0.1 GPa to 8.7 GPa. **b** XRD pattern at 2.0 GPa. The peaks are indexed to the cubic phase of BaF_2. **c** The XRD pattern at 3.7 GPa reveals the phase transition from the cubic to orthorhombic phase. **d** XRD patterns at 4.5 GPa. The peaks are indexed to the orthorhombic phase of BaF_2.

sharing interactions. The atomic coordinates are (0.25, 0.115, 0.25), (0.36, 0.43, 0.25), and (0.028, 0.333, 0.75) for Ba, F_1 and F_2, respectively. The lattice constants at the onset of the orthorhombic phase are $a = 6.63$ Å, $b = 7.71$ Å, and $c = 3.92$ Å (Fig. 2b). Figure 4c reveals that at 3.7 GPa, a phase change from cubic to orthorhombic is imminent, as the XRD pattern contains peaks that can be indexed to both cubic and orthorhombic phases[22,23]. For both the cubic and orthorhombic phases, the lattice constants decrease as the BaF_2 crystal is compressed by increasing pressure, as shown in Fig. 5. Numerical simulations for pressures up to 14 GPa agree well with the experimental lattice constants, particularly with the decrease in the lattice constants as the pressure increases. The experimental results are limited to pressures less than 8.7 GPa since the sapphire anvil cell was unable to withstand higher pressures.

The calculated band structures of BaF_2 for the different pressures applied in the experiments are shown in Fig. 6. Table 1 summarizes the energy gaps between the valence and conduction bands (valence–conduction bandgap), the core–conduction bandgap, and the core–valence bandgap. In the cubic phase, when the applied pressure is less than 3.7 GPa, the valence–conduction bandgap appears to be stable. The valence–conduction bandgap slightly increases with increasing pressure in the orthorhombic phase. Nevertheless, the conduction and valence bands do not appear to dramatically flatten even as the crystal is compressed. A major requirement for CL is that the valence −conduction bandgap should be greater than the core −valence bandgap so that the CL photons are not reabsorbed by the material. Band gap control and band structure manipulation through uniform and uniaxial pressure application were previously demonstrated in hexagonal lithium calcium aluminum fluoride (LiCaAlF or LiCAF)[26] and lithium yttrium fluoride ($YLiF_4$)[27] laser materials. Uniform volume compression at increasing pressures up to 50 GPa monotonically increased the

valence−conduction bandgap of LiCAF because of the flattening of the conduction band. Luminescence from LiCAF was, however, not observed. The core−conduction bandgap of BaF_2 slightly increases as the crystal structure changes from cubic to orthorhombic. In most applications that require a fast-response scintillator, the radiation being measured has enough energy to promote an electron across the 14–15 eV energy gap between the core and conduction bands. Therefore, a slight increase in the core−conduction bandgap will hardly affect the performance of the scintillator. Interestingly, the core−valence bandgap decreases as the pressure increases, as observed in Fig. 6. Increasing the pressure introduces a tensile strain that expands the valence band downward. The decrease in the core−valence bandgap is more obvious in the orthorhombic phase at high pressures, as the downward expansion of the valence band is more pronounced. For all pressures considered, the core−valence bandgap is always less than the valence−conduction bandgap (Table 1). Therefore, self-absorption of CL emission is avoided, even at high pressures. Moreover, the decrease in the core−valence bandgap alludes to the exciting prospect of shifting the CL emission to longer wavelengths.

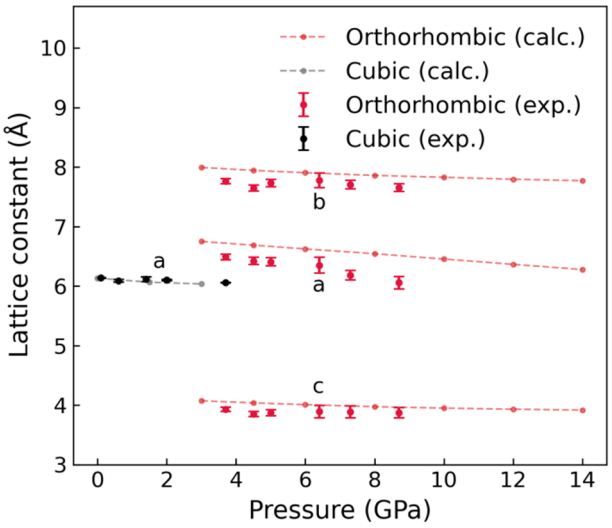

Fig. 5 Lattice constants. Experimental (plots with error bars) and calculated (plots with dashed lines) lattice constants for the cubic and orthorhombic phases of BaF_2 at pressures from 0 GPa to 14 GPa. The error bars indicate standard deviations.

Figure 7a shows the experimentally obtained luminescence emission spectra of BaF_2 under pressures ranging from 0.1 GPa to 8.7 GPa. The resolution of the luminescence spectra is 0.2 nm. The spectra presented were corrected according to the spectral response of the spectrometer. Figure 7e and f shows the decomposition of the luminescence emission spectra into Gaussian components. The peak at ~220 nm arises from CL emission, whereas the peak at ~300 nm comes from STE emission. The energy of the CL and STE emission peaks, determined from the peak energy of the Gaussian components, as the pressure increases are shown in Fig. 7g and

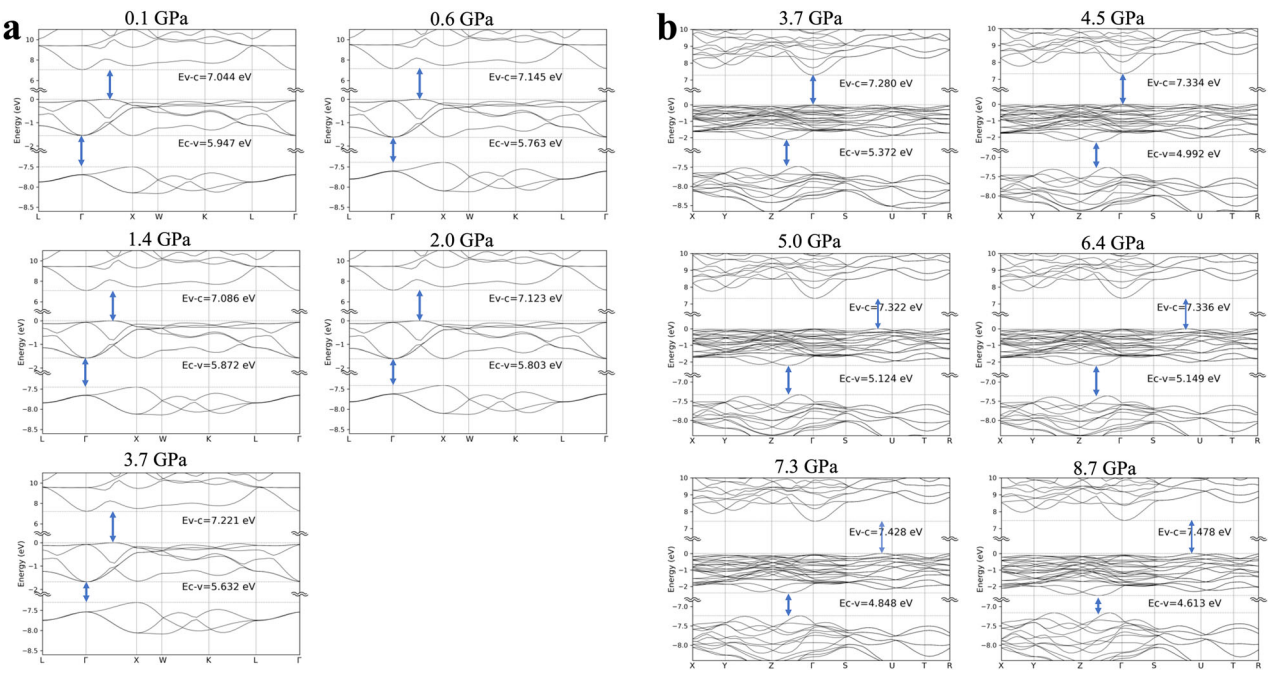

Fig. 6 Calculated band structures of BaF_2. a Cubic phase at pressures from 0.1 GPa to 3.7 GPa. **b** Orthorhombic phase at pressures ranging from 3.7 GPa to 8.7 GPa.

Table 1 Summary of the calculated energy gaps.

Pressure (GPa)	Crystal phase	Ev−c (eV)	Ec−v (eV)	Ec−c (eV)	ΔE_v (eV)
0.1	Cubic	7.044 (indirect)	5.947 (indirect)	14.544 (indirect)	1.56
0.6	Cubic	7.145 (indirect)	5.763 (indirect)	14.533 (indirect)	1.60
1.4	Cubic	7.086 (indirect)	5.872 (indirect)	14.539 (indirect)	1.61
2.0	Cubic	7.123 (indirect)	5.803 (indirect)	14.534 (indirect)	1.65
3.7	Cubic	7.143 (indirect)	5.632 (indirect)	14.451 (indirect)	1.67
3.7	Orthorhombic	7.280 (direct)	5.372 (indirect)	14.761 (indirect)	2.11
4.5	Orthorhombic	7.334 (direct)	4.992 (indirect)	14.597 (indirect)	2.27
5.0	Orthorhombic	7.322 (indirect)	5.124 (indirect)	14.657 (indirect)	2.21
6.4	Orthorhombic	7.336 (indirect)	5.149 (indirect)	14.698 (indirect)	2.21
7.3	Orthorhombic	7.428 (indirect)	4.848 (indirect)	14.668 (indirect)	2.39
8.7	Orthorhombic	7.478 (indirect)	4.613 (indirect)	14.639 (indirect)	2.55

Ev−c, Ec−v, and Ec−c indicate the energy gaps between the valence and conduction bands (valence–conduction bandgap), the core and valence bands (core–valence bandgap), and the core and conduction bands (core–conduction bandgap), respectively. ΔE_v is the width of the valence band used to indicate how much the 2*p* F^- valence band has broadened.

summarized in Table 2. The wavelengths and energies of the CL and STE emission peaks, as well as the valence−conduction and core−valence bandgaps, are shown in Fig. 7b. The data points in Fig. 7b, which refer to the experimental data (solid lines), are the same values as those plotted in Fig. 7g. The CL spectra should extend up to 7.1 eV[28], but the fiber spectrometer used in the experiment can measure only up to 200 nm. In the cubic phase, the STE luminescence peak appears to be blue-shifted as the pressure increases from 0.1 to 3.7 GPa. The shift to shorter wavelengths (open black squares in Fig. 7b) is consistent with the increase in the valence−conduction bandgap (open gray squares in Fig. 7b; Table 1). The STE luminescence intensity initially increases as the pressure increases to 1.4 GPa. As the pressure further increases, the STE luminescence intensity decreases. Figure 7c and d shows the luminescence spectra at 3.7 GPa and 6.4 GPa, respectively. At 3.7 GPa, when BaF_2 exists in both the cubic and orthorhombic phases and the phase transition to orthorhombic phases is imminent, both the CL peak at 220 nm and the STE peak at 300 nm are present, but the STE peak is more intense. At 6.4 GPa, when BaF_2 exists in the orthorhombic phase, both the CL peak at 220 nm and the STE peak at 300 nm are also present, but the CL peak is more intense. Therefore, the luminescence peak observed at pressures greater than 4.5 GPa in Fig. 7a is due to CL. The total density of states and partial density of states of BaF_2 in the cubic and orthorhombic phases and increasing pressures are shown in Fig. 8. In all the cases, the core band is derived predominantly from the 5*p* orbital of Ba^{2+}, the valence band is derived predominantly from the 2*p* orbital of F^-, and the conduction band is derived from the 5*d* orbital of Ba^{2+}. These orbital compositions of the core, valence, and conduction bands satisfy the conditions for CL, further confirming that the luminescence peak observed at high pressures (Fig. 7a) is due to CL. When the incident 20 keV X-rays excite the BaF_2 crystal, high-energy electrons, and holes are created in the crystal via electrons transitioning from the 5*p* Ba^{2+} core band to the 6*s*, 5*d* Ba^{2+} conduction band and subsequently from the 2*p* F^- valence band to the 5*p* Ba^{2+} core band. As the holes lose energy through thermalization, the holes become localized in the form of V_k centers (self-trapped holes). The radiative recombination of the conduction band electrons and the self-trapped holes results in STE luminescence emission. The increase in the intensity of STE emission indicates that the radiative decay of the STE (electron−hole) is enhanced at low pressures. Since the number of STEs formed depends on the quantity of electrons and holes[29], it is plausible that low-pressure application up to 1.4 GPa increases the density of electrons and holes as the unit cell volume is reduced following the decrease in the lattice constant. As previously observed in Nd^{3+}:$SrWO_4$ and $InNbO_4$ crystals, a reduction in the unit cell volume increases the effective concentration of ions involved in radiative processes, increasing the efficiency of energy transfer processes[30,31]. In these works, a reduction in the unit cell volume was achieved by doping. The reduction in the unit cell volume due to dopants is equivalent to an externally applied pressure of 1.14 GPa[30], which is similar to the 1.4 GPa maximum applied pressure for which the intensity of the STE emission from BaF_2 increased. A further compression of the crystal using pressures greater than 1.4 GPa increased the valence−conduction bandgap. These structural changes perturb the V_k centers. The perturbed

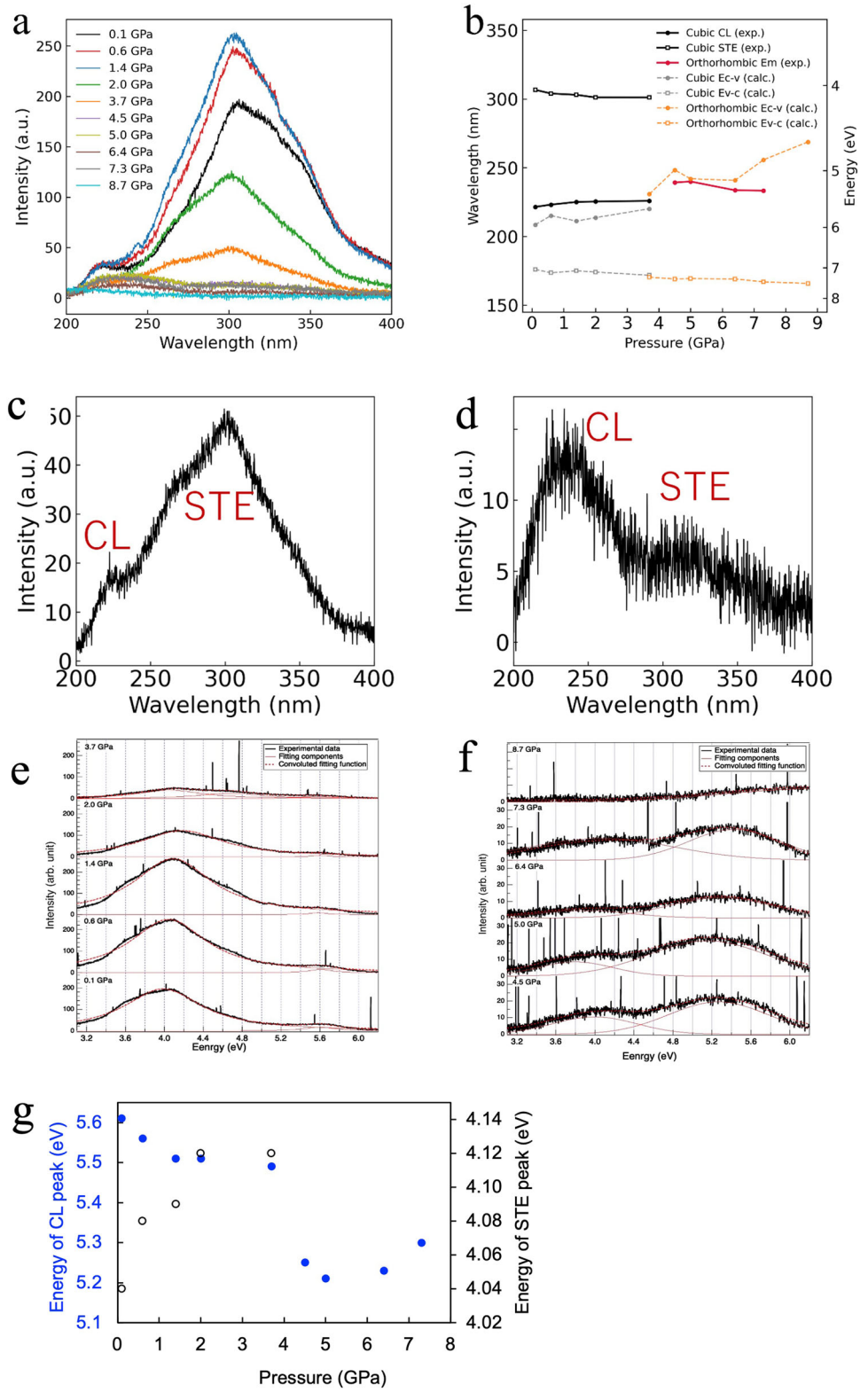

Fig. 7 (See legend on next page.)

(see figure on previous page)
Fig. 7 Luminescence spectra and wavelength shifts. a Luminescence emission spectra of BaF_2 under pressures ranging from 0.1 GPa to 8.7 GPa. The peak at ~220 nm arises from CL emission, whereas the peak at ~300 nm comes from STE recombination. **b** Wavelengths of the CL and STE emission peaks, as well as the valence–conduction and core–valence bandgaps of BaF_2 under pressures ranging from 0.1 GPa to 8.7 GPa. Luminescence spectra at (**c**) 3.7 GPa (cubic and orthorhombic phases) showing both CL and STE emission, with the STE emission being more intense, and (**d**) 6.4 GPa (orthorhombic phase) showing both CL and STE emission, with the CL emission being more intense. The spectra are normalized to the same intensity scale. (**e**) and (**f**) Luminescence spectra fit to Gaussian components of the CL and STE peaks at each pressure. **g** Shift in the CL (solid blue circles) and STE (hollow black circles) peaks as a function of pressure.

Table 2 Summary of the cross-luminescence and self-trapped exciton peaks.

Pressure (GPa)	Phase	CL peak position (nm)	CL peak position (eV)	STE peak position (nm)	STE peak position (eV)
0.1	Cubic	221	5.61	307	4.04
0.6	Cubic	223	5.56	304	4.08
1.4	Cubic	225	5.51	303	4.09
2.0	Cubic	225	5.51	301	4.12
3.7	Cubic	226	5.49	301	4.12
4.5	Orthorhombic	236	5.25		
5.0	Orthorhombic	238	5.21		
6.4	Orthorhombic	237	5.23		
7.3	Orthorhombic	234	5.30		

V_k centers did not efficiently take part in the radiative STE recombination process, leading to a decrease in the intensity of the STE emission. A similar phenomenon was observed in BaF_2 doped with cadmium[32,33] and lanthanum[34,35] ions, where the self-trapped holes associated with charge-compensating interstitial fluoride ions formed additional V_k-type centers that participated in nonradiative conduction band electron−localized hole recombination, thereby suppressing STE emission. The decrease in the STE intensity of La(1%)-doped BaF_2 is ~61% compared with that of undoped BaF_2 and ~98% for La(10%)-doped BaF_2. At both the 1% and 10% doping concentrations, the intensity of CL emission remains unchanged. A La doping concentration of 20% results in the suppression of the STE but also in a decrease of ~87% in the CL intensity, as estimated from the data presented in reference 33. On the other hand, a decrease in the STE intensity of ~38% was observed at a 2.0 GPa applied pressure compared with the STE intensity at ambient pressure, whereas the intensity of the CL emission remained unchanged. Above 3.7 GPa, the STE intensity is suppressed, but the CL intensity decreases by ~28%. The suppression of STE emission was also reported in BaF_2 doped with strontium and magnesium ions[36]. In this case, the dopant ions act as electron-trapping centers. At the phase transition from cubic to orthorhombic (3.7 GPa), the complete structural change and increase in the valence−conduction bandgap inhibited the recombination of conduction band electrons and self-trapped holes, leading to the suppression of STE emission. In all previous works, STE emission was suppressed via the introduction of a dopant ion. Our results show that STE emissions can also be suppressed by high-pressure applications. In the orthorhombic phase, at pressures greater than 3.7 GPa, the valence−conduction bandgap further increases monotonically with pressure (see Table 1). The increased valence−conduction bandgap could have continued to inhibit the recombination of conduction band electrons and self-trapped holes, resulting in the continued suppression of STE emission. Further high-pressure experiments at the orthorhombic phase are needed to fully ascertain the origin of the change in the properties of STE luminescence compared with those of the cubic phase.

In the cubic phase, the CL emission peak at 221 nm slightly redshifts to 226 nm as the pressure increases from 0.1 GPa to 3.7 GPa. The shift to longer wavelengths of the CL peak (solid black circles in Fig. 7b) is consistent with the decrease in the core−valence bandgap (solid gray circles in Fig. 7b; Table 1) for cubic BaF_2 under pressure. The intensity of CL emission appears to be constant as the pressure is increased. At 3.7 GPa, where BaF_2 exists in both the cubic and orthorhombic phases, the luminescence emission intensity is weakened. In the orthorhombic phase, the luminescence emission intensity appears to be stable, albeit weaker than the intensity in the cubic phase, as the pressure increases. Interestingly, the luminescence peak clearly shifts to a longer wavelength by the phase transition from the cubic phase to the

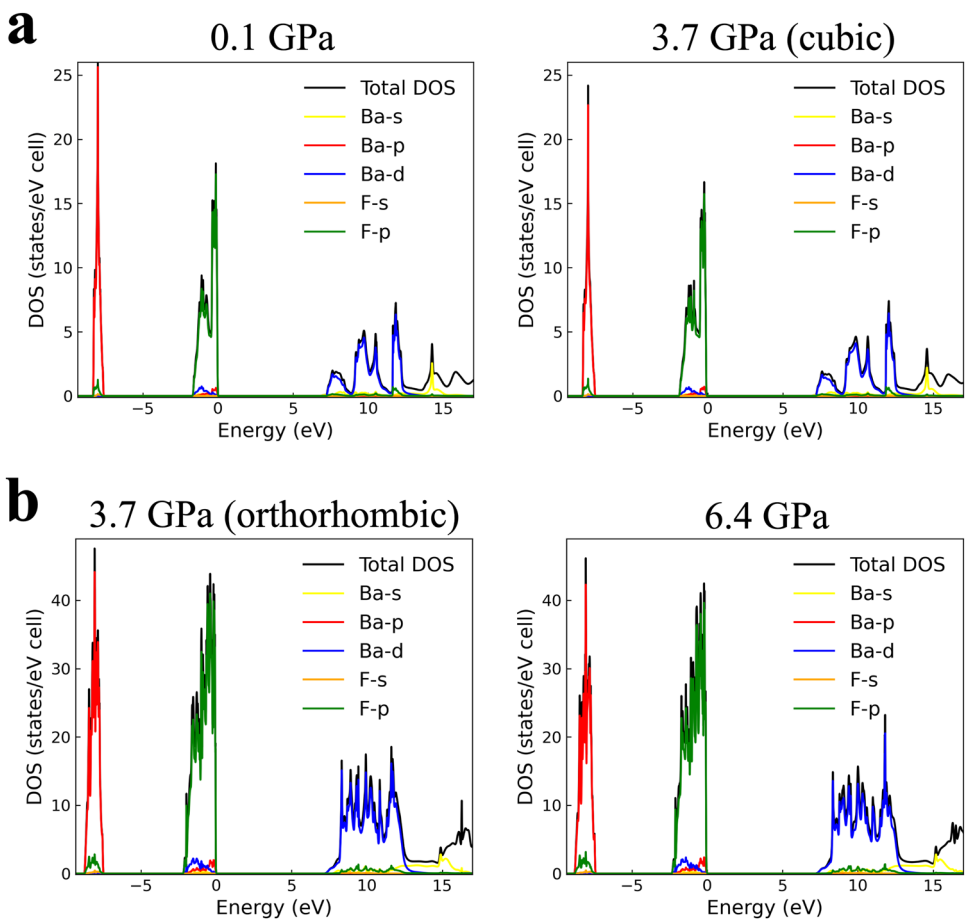

Fig. 8 Partial and total density of states. a Cubic phase. **b** Orthorhombic phase.

orthorhombic phase (solid circles with solid lines in Fig. 7b, replotted as solid circles in Fig. 7g; Table 2). At an applied pressure of 5.0 GPa, a maximum shift to 238 nm is observed. This shift is consistent with the decrease in the core−valence bandgap in the orthorhombic phase due to the downshift of the valence band (solid orange circles with dashed lines in Fig. 7b; Table 1). The observed broadening of the luminescence emission, especially in the orthorhombic phase, could be attributed to the expansion of the valence bandwidth as the pressure increases. As shown in Table 1, the width of the valence band (ΔE_v) increases monotonically as the pressure increases. At high pressure, the strengthened crystal field can induce greater band splitting and enhance electron–phonon coupling[37]. Indeed, previous works have reported similar broadening in valence−conduction band photoluminescence emission[38–40], but this is the first report on broadening of core−valence band luminescence. The experimental and calculation results suggest that high-pressure application modifies the electronic structure of BaF_2, alluding to exciting prospects for tunable CL emission. The decrease in the energy gap between the core and valence bands as BaF_2 is compressed under high pressure shifts the CL emission peak to longer wavelengths. A phase shift from cubic to orthorhombic is observed at an applied pressure of ~3.7 GPa. In the orthorhombic phase, STE luminescence disappears, and the CL emission peak broadens. Compared with CL, STE luminescence is a slower process. Hence, several schemes have been used to suppress STE luminescence, including doping BaF_2 with cadmium and lanthanum ions[33]. Our results suggest that subjecting the crystal to high pressure could be an alternative solution for suppressing STE luminescence along with increasing the CL wavelength. As mentioned previously, doping with 1% lanthanum led to a 61% decrease in the STE luminescence intensity compared with undoped BaF_2. In the case of high-pressure application, the STE luminescence intensity decreased by 38% at an applied pressure of 2.0 GPa compared with that under ambient conditions. High pressure could also potentially be applied to other fast-response scintillators that emit short vacuum ultraviolet wavelengths (VUV, wavelength range from 100 nm to 200 nm) that are difficult to detect. Many VUV-emitting

materials, especially compound fluorides doped with trivalent neodymium and erbium ions[41–47], have been investigated and reported as fast-response scintillators with typical decay times of a few nanoseconds because the decay time is directly correlated with the luminescence emission wavelength. This means that the shorter the luminescence wavelength is, the faster the decay time[48].

In summary, we numerically and experimentally determined the evolution of the STE and CL emissions observed from BaF_2 under pressure. The phase transition from cubic to orthorhombic at ~3.7 GPa results in the suppression of slow STE luminescence emission. At applied pressures greater than 3.7 GPa, the CL intensity decreases by ~28%. The downshift in the valence bands results in narrowing of the core−valence bandgap, which is magnified in the orthorhombic phase at high pressure. The narrowing of the core−valence bandgap results in the shifting of the CL emission peak to longer wavelengths. This result alludes to the prospect of using high pressure to aid in the detection of otherwise difficult-to-detect wavelengths in the VUV region.

Methods

In situ luminescence and XRD spectra measurements under high pressure

The experiments were conducted at the BL-18C beamline in the Photon Factory (KEK, Tsukuba, Japan). The temperature condition was room temperature. The experimental schematic diagram is shown in Fig. 3a. An X-ray beam with a photon energy of 20 keV and a beam diameter of 100 μm was incident on the BaF_2 sample, and most of the X-rays were absorbed by the sample. The luminescence of the sample was measured by a spectrometer (HORIBA iHR 320) through an optical fiber. The spectrometer has a grating density of 600 g/mm. The X-ray diffraction (XRD) pattern was measured by moving the flat panel detector behind the sample with a camera length of 139 mm. The sample was subjected to pressure in a sapphire anvil cell (Fig. 3b). A pair of anvils applied pressure to the sample, and the pressure on the sample was increased by closing four screws on the cell. The diameter of the sapphire anvil cell was 3.10 mm, the height was 1.70 mm, and the culet diameter was 0.80 mm. The space around the sample was filled with a pressure-transmitting medium, which was a liquid mixture of 4:1 methanol and ethanol. The liquid mixture maintains a hydrostatic pressure of ~10 GPa at room temperature[49]. The pressure value was observed by measuring the emission spectrum from a ruby ball. How the ruby luminescence wavelength shifts with external pressure has been previously reported[50–52]. The hole diameter of the copper gasket was 300 μm. Copper is usually used as the gasket material for sapphire anvils[53].

Numerical calculations

The effects of increasing pressure on the electronic properties of BaF_2 were investigated numerically through the uniform compression of the lattice constants achieved by applying Pulay stress along both axes of the crystal. The pressures considered in the numerical calculations ranged from 0.1 GPa (approximately ambient) to 14 GPa, following the pressure values in the experiment up to 8.7 GPa. The atomic coordinates and lattice constants were optimized for each pressure. The optimized lattice constants for each pressure were used for band structure calculations. A convergence criterion of 1×10^{-6} eV/atom and a sufficiently high plane wave basis cutoff of 500 eV were imposed for geometry optimization and band structure calculation via the generalized gradient approximation and Perdew–Burke–Ernzerhof (GGA–PBE) functional. The *k*-point paths for band structure calculations for cubic and orthorhombic structures were set following the first Brillouin zone[21,54,55].

Acknowledgements

This research was supported by JSPS KAKENHI Grant Numbers JP21K18909 and JP23K13047 and Osaka University, Institute of Laser Engineering Collaborative Research Fund (2023B1-003, 2024B1-008). The authors would like to acknowledge the Centre for Theoretical Chemistry and Physics, Massey University, for their technical support in using the SIMURG high-performance computing cluster. The experiments were performed at the BL-18C beamline of the Photon Factory (Proposal No. 2022P004).

Author details

[1]Unitec Institute of Technology, 139 Carrington Road, Mount Albert, Auckland 1025, New Zealand. [2]Institute of Laser Engineering, Osaka University, 2-6 Yamadaoka, Suita, Osaka 565-0871, Japan. [3]Centre for Theoretical Chemistry and Physics, Massey University, Auckland 0632, New Zealand. [4]Graduate School of Engineering, Osaka University, 2-1 Yamadaoka, Suita, Osaka 565-0871, Japan. [5]Institute of Materials Structure Science, High Energy Accelerator Research Organization (KEK), Tsukuba 305-0801, Japan. [6]New Industry Creation Hatchery Center, Tohoku University, 6-6-10 Aoba, Aramaki, Aoba-ku, Sendai, Miyagi 980-8579, Japan

Author contributions

M.C.-R. conceived the idea of applying high pressure to shift the CL wavelength, interpreted the data, wrote the manuscript, and contributed equally to research planning. L.V.M. supervised the numerical simulations, performed some of the simulations, and wrote the numerical simulation method. M.Y. performed the experiments and some numerical simulations, plotted the results, and wrote the experimental methods. Y.S. designed and performed the experiments and provided technical support. T.S. gave conceptual advice on this work. N.S. obtained research funding, gave conceptual advice, and contributed equally to research planning. K.Y. designed and supervised the experiments, obtained research funding, interpreted the data, and contributed equally to research planning. All authors discussed and analyzed the results and commented on the manuscript at all stages.

Data availability

The data that support the findings of this study are available from the corresponding author upon request.

Code availability

All the calculations were performed with the CASTEP code. The code is available from the corresponding author upon request.

Conflict of interest

The authors declare no competing interests.

Received: 5 April 2024 Revised: 17 July 2024 Accepted: 1 August 2024.
Published online: 11 October 2024

References

1. Nikl, M. Scintillation detectors for x-rays. *Meas. Sci. Technol.* **17**, R37 (2006).
2. Arikawa, Y. et al. Note: Light output enhanced fast response and low afterglow ^{6}Li glass scintillator as potential down-scattered neutron diagnostics for inertial confinement fusion. *Rev. Sci. Instrum.* **81**, 106105 (2010).
3. Murata, T. et al. Fast-response and low-afterglow cerium-doped lithium 6 fluoro-oxide glass scintillator for laser fusion-originated down-scattered neutron detection. *IEEE Trans. Nucl. Sci.* **59**, 2256–2259 (2012).
4. Nakazato, T. et al. Systematic study on Ce:$LuLiF_4$ as a fast scintillator using storage ring free-electron lasers. *Jpn. J. Appl. Phys.* **49**, 122602 (2010).
5. Empizo, M. J. F. et al. Spectroscopic properties of Pr^{3+}-doped 20$Al(PO_3)_3$-80LiF glasses as potential scintillators for neutron detection. *J. Lumin.* **193**, 13–21 (2018).
6. Watanabe, K. et al. Pr or Ce-doped, fast-response and low-afterglow cross-section-enhanced scintillator with ^{6}Li for down-scattered neutron originated from laser fusion. *J. Cryst. Growth* **362**, 288–290 (2013).
7. Tsuboi, M. et al. Electronic states of trivalent praseodymium ion doped in 20$Al(PO_3)_3$-80LiF glass. *Jpn. J. Appl. Phys.* **52**, 062402 (2013).
8. Yamanoi, K. et al. Luminescence Properties of Nd^{3+}-Doped AlF_3-Based Fluoride Glass in the Vacuum Ultraviolet Region. *Phys. Status Solidi B* **257**, 1900475 (2020).
9. Makhov, V. Vacuum ultraviolet luminescence of wide band-gap solids studied using time-resolved spectroscopy with synchrotron radiation. *Phys. Scr.* **89**, 044010 (2014).
10. Lewellen, T. K. Time-of-flight PET. *Semin. Nucl. Med.* **28**, 268–275 (1998).
11. Arikawa, Y. et al. Development of multichannel low-energy neutron spectrometer. *Rev. Sci. Instrum.* **85**, 11E125 (2014).
12. Empizo, M. J. F. et al. Investigations on the electric-dipole allowed $4f^{2}5d \rightarrow 4f^{3}$ broadband emission of Nd^{3+}-doped 20$Al(PO_3)_3$-80LiF glass for potential VUV scintillator application. *J. Alloy. Compd.* **856**, 158096 (2021).
13. Minami et al. Spectroscopic investigation of praseodymium and cerium co-doped 20$Al(PO_3)_3$-80LiF glass for potential scintillator applications. *J. Non-Cryst. Solids* **521**, 119495 (2019).
14. Van Eijk, C. W. E. Cross-luminescence. *J. Lumin* **60–61**, 936–941 (1994).
15. Cadatal-Raduban, M. et al. Investigation of cross luminescence in lanthanum fluoride as a potential fast-response scintillator. *Jpn. J. Appl. Phys.* **59**, 052005 (2020).
16. Yamanoi, K. et al. Perovskite fluoride crystals as light emitting materials in vacuum ultraviolet region. *Opt. Mater.* **36**, 769–772 (2014).
17. Cadatal-Raduban, M. et al. Tunable vacuum ultraviolet cross-luminescence from $KMgF_3$ under high pressure as potential fast-response scintillator. *J. Chem. Phys.* **154**, 124707 (2021).
18. Laval, M. et al. Barium fluoride—inorganic scintillator for subnanosecond timing. *Nucl. Instrum. Methods Phys. Res* **206**, 169–176 (1983).
19. Omelkov, S. I. et al. Recent advances in time-resolved luminescence spectroscopy at MAX IV and PETRA III storage rings. *J. Phys. Conf. Ser.* **2380**, 012135 (2022).
20. Gundacker, S. et al. Vacuum ultraviolet silicon photomultipliers applied to BaF_2 cross-luminescence detection for high-rate ultrafast timing applications. *Phys. Med. Biol.* **66**, 114002 (2021).
21. Woody, C. L. & Anderson, D. F. Calorimetry using BaF_2 with photosensitive wire chamber readout. *Nucl. Instrum. Methods Phys. Res. Sect. A* **265**, 291–300 (1988).
22. Kanchana, V., Vaitheeswaran, G. & Rajagopalan, M. Pressure induced structural phase transitions and metallization of BaF_2. *J. Alloy. Compd.* **359**, 66–72 (2003).
23. Leger, J. M., Haines, J., Atouf, A., Schulte, O. & Hull, S. High-pressure x-ray- and neutron-diffraction studies of BaF_2: An example of a coordination number of 11 in AX_2 compounds. *Phys. Rev. B Condens. Matter* **52**, 13247 (1995).
24. Smith, J. S. et al. High-pressure structures and vibrational spectra of barium fluoride: Results obtained under nearly hydrostatic conditions. *Phys. Rev. B Condens. Matter* **79**, 134104 (2009).
25. Lu, H.-C. et al. Photoluminescence of a CVD diamond excited with VUV light from a synchrotron. *Opt. Photonics J.* **3**, 25–28 (2013).
26. Heath, D. F. & Sacher, P. A. Effects of a simulated high-energy space environment on the ultraviolet transmittance of optical materials between 1050 Å and 3000 Å. *Appl. Opt.* **5**, 937–944 (1966).
27. Shimizu, T. et al. High pressure band gap modification of $LiCaAlF_6$. *Appl. Phys. Lett.* **110**, 141902 (2017).
28. Rodnyi, P. A. Core-valence luminescence in scintillators. *Radiat. Meas.* **38**, 343 (2004).
29. Luong, M. V. et al. Direct band gap tunability of the $LiYF_4$ crystal through high-pressure applications. *Comput. Mater. Sci.* **153**, 431–437 (2018).
30. Biasini, M., Cassidy, D. B., Deng, S. H. M., Tanaka, H. K. M. & Mills, A. P. Suppression of the slow component of scintillation light in BaF_2. *Nucl. Instrum. Methods Phys. Res. Sect. A* **553**, 550–558 (2005).
31. Botella, P. et al. Investigation on the luminescence properties of $InMO_4$ (M = V^{5+}, Nb^{5+}, Ta^{5+}) crystals doped with Tb^{3+} or Yb^{3+} rare earth ions. *ACS Omega* **5**, 2148–2158 (2020).
32. Errandonea, D. et al. Effect of pressure on the luminescence properties of Nd^{3+} doped $SrWO_4$ laser crystal. *J. Alloy. Compd.* **451**, 212–214 (2008).
33. Nepomnyashchikh, A. I. et al. Defect formation in BaF_2 crystals doped with cadmium. *Nucl. Instrum. Methods Phys. Res., Sect. A* **537**, 27–30 (2005).
34. Nepomnyashchikh, A. I., Radzhabov, E. A., Egranov, A. V., Ivashechkin, V. F. & Istomin, A. S. Recombination processes in crystals of solid solutions of $Ba_{1-x}La_xF_{2+x}$. *Nucl. Instrum. Methods Phys. Res. Sect. A* **486**, 390–394 (2002).
35. Schotanus, P., Dorenbos, P., van Eijk, C. W. E. & Hollander, R. W. Recent developments in scintillator research. *IEEE Trans. Nucl. Sci.* **36**, 132–136 (1989).
36. Hamada, M. M., Nunoya, Y., Sakuragui, S. & Kubota, S. Suppression of the slow component of BaF_2 crystal by introduction of SrF_2 and MgF_2 crystals. *Nucl. Instrum. Methods Phys. Res. Sect. A* **353**, 33–36 (1994).
37. Runowski, M., Woźny, P., Stopikowska, N., Guo, Q. & Lis, S. Optical pressure sensor based on the emission and excitation band width (fwhm) and luminescence shift of Ce^{3+}-doped fluorapatite—high-pressure sensing. *ACS Appl. Mater. Interfaces* **11**, 4131–4138 (2019).
38. Meng, X. et al. Pressure-dependent behavior of defect-modulated band structure in boron arsenide. *Adv. Mater.* **32**, 2001942 (2020).
39. Nayak, A. P. et al. Pressure-dependent optical and vibrational properties of monolayer molybdenum disulfide. *Nano Lett.* **15**, 346–353 (2015).
40. Barzowska, J., Lesniewski, T., Mahlik, S., Seo, H. J. & Grinberg, M. $KMgF_3$:Eu^{2+} as a new fluorescence-based pressure sensor for diamond anvil cell experiments. *Opt. Mater.* **84**, 99–102 (2018).
41. Cadatal-Raduban, M. et al. Vacuum ultraviolet luminescence from a micro-pulling-down method grown Nd:$(La_{0.9},Ba_{0.1})F_{2.9}$. *J. Lumin.* **129**, 1629–1631 (2009).
42. Nakazato, T. et al. Nd^{3+}:LaF_3 as a step-wise excited scintillator for femtosecond ultraviolet pulses. *IEEE Trans. Nucl. Sci.* **57**, 1208–1210 (2010).
43. Cadatal-Raduban, M. et al. Vacuum ultraviolet optical properties of a micro-pulling-down-method grown Nd^{3+}: $(La_{0.9}, Ba_{0.1})F_{2.9}$. *J. Opt. Soc. Am. B Opt. Phys.* **25**, 27–31 (2008).
44. Cadatal-Raduban, M. et al. Nd^{3+}:$(La_{1-x}Ba_x)F_{3-x}$ grown by micro-pulling down method as vacuum ultraviolet scintillator and potential laser material. *Jpn. J. Appl. Phys.* **46**, L985 (2007).
45. Cadatal-Raduban, M. et al. Micro-pulling down method-grown Er^{3+}:$LiCaAlF_6$ as prospective vacuum ultraviolet laser material. *J. Cryst. Growth* **362**, 167–169 (2013).
46. Yamanoi, K. et al. VUV fluorescence from Nd^{3+}:$LuLiF_4$ by two photon excitation using femtosecond laser. *Opt. Mater.* **35**, 2030–2033 (2013).
47. Shinzato, Y. et al. Vacuum ultraviolet fluorescence spectroscopy of Nd^{3+}:LaF_3 using femtosecond extreme ultraviolet free electron laser. *Appl. Phys. Express* **6**, 022401 (2013).
48. Yanagida, T. et al. Study of the correlation of scintillation decay and emission wavelength. *Radiat. Meas.* **55**, 99–102 (2013).
49. Piermarini, G. J., Block, S. & Barnett, J. D. Hydrostatic limits in liquids and solids to 100 kbar. *J. Appl. Phys.* **44**, 5377–5382 (1973).
50. Mao, H. K., Bell, P. M., Shaner, J. W. & Steinberg, D. J. Specific volume measurements of Cu, Mo, Pd, and Ag and calibration of the ruby R_1 fluorescence pressure gauge from 0.06 to 1 Mbar. *J. Appl. Phys.* **49**, 3276–3283 (1978).

51. Mao, H. K., Xu, J. & Bell, P. M. Calibration of the ruby pressure gauge to 800 kbar under quasi-hydrostatic conditions. *J. Geophys. Res. Solid Earth* **91**, 4673–4676 (1986).
52. Zha, C.-S., Mao, H.-K. & Hemley, R. J. Elasticity of MgO and a primary pressure scale to 55 GPa. *PNAS* **97**, 13494–13499 (2000).
53. Furuno, K., Onodera, A. & Kume, S. Sapphire-anvil cell for high pressure research. *Jpn. J. Appl. Phys.* **25**, L646 (1986).
54. Jiang, H., Pandey, R., Darrigan, C. & Rerat, M. First-principles study of structural, electronic and optical properties of BaF_2 in its cubic, orthorhombic and hexagonal phases. *J. Phys. Condens. Matter* **15**, 709–718 (2003).
55. Yang, X., Hao, A., Wang, X., Liu, X. & Zhu, Y. First-principles study of structural stabilities, electronic and elastic properties of BaF_2 under high pressure. *Comput. Mater. Sci.* **49**, 530–534 (2010).